

Graphene kirigami

Melina K. Bles¹, Arthur W. Barnard², Peter A. Rose¹, Samantha P. Roberts¹, Kathryn L. McGill¹, Pinshane Y. Huang², Alexander R. Ruyack³, Joshua W. Kevek¹, Bryce Kobrin¹, David A. Muller^{2,4} & Paul L. McEuen^{1,4}

For centuries, practitioners of origami ('ori', fold; 'kami', paper) and kirigami ('kiri', cut) have fashioned sheets of paper into beautiful and complex three-dimensional structures. Both techniques are scalable, and scientists and engineers are adapting them to different two-dimensional starting materials to create structures from the macro- to the microscale^{1,2}. Here we show that graphene^{3–6} is well suited for kirigami, allowing us to build robust microscale structures with tunable mechanical properties. The material parameter crucial for kirigami is the Föppl–von Kármán number^{7,8} γ : an indication of the ratio between in-plane stiffness and out-of-plane bending stiffness, with high numbers corresponding to membranes that more easily bend and crumple than they stretch and shear. To determine γ , we measure the bending stiffness of graphene monolayers that are 10–100 micrometres in size and obtain a value that is thousands of times higher than the predicted atomic-scale bending stiffness. Interferometric imaging attributes this finding to ripples in the membrane^{9–13} that stiffen the graphene sheets considerably, to the extent that

γ is comparable to that of a standard piece of paper. We may therefore apply ideas from kirigami to graphene sheets to build mechanical metamaterials such as stretchable electrodes, springs, and hinges. These results establish graphene kirigami as a simple yet powerful and customizable approach for fashioning one-atom-thick graphene sheets into resilient and movable parts with microscale dimensions.

Devices such as those shown in Fig. 1a, c, d are made from polycrystalline monolayer graphene that is grown on copper by chemical vapour deposition¹⁴, and then transferred to fused silica wafers that are covered with an aluminium release layer. We use optical lithography to pattern both the graphene and the 50-nm-thick gold pads that are deposited on top of the graphene to act as handles. Finally, we release the graphene from the surface by etching away the aluminium in mild acid. The devices remain in aqueous solution with added salts or surfactants as desired. An inverted white-light microscope with a video camera is used to image the sheets, and micromanipulators are used to probe them.

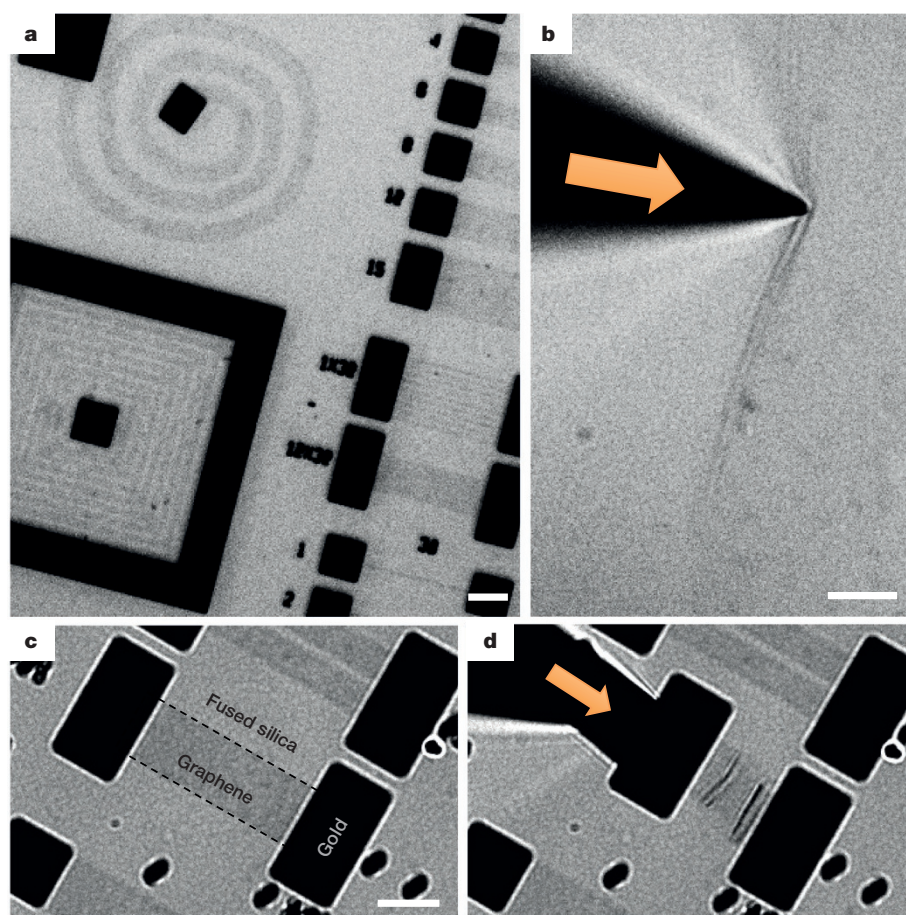


Figure 1 | Patterning and manipulating graphene. **a**, Transmission white-light image showing completed devices: a spiral spring, a kirigami pyramid, and a variety of cantilevers. **b**, Manipulating a large sheet of graphene with a micromanipulator. The sheet folds and crumples like soft paper, and returns to its original shape. **c**, **d**, Manipulating devices with gold pads. The devices can be lifted entirely off the surface; see Supplementary Video 1. Scale bars are 10 μm . All images and videos have undergone linear contrast adjustments.

¹Laboratory of Atomic and Solid State Physics, Cornell University, Ithaca, New York 14853, USA. ²School of Applied and Engineering Physics, Cornell University, Ithaca, New York 14853, USA. ³School of Electrical and Computer Engineering, Cornell University, Ithaca, New York 14853, USA. ⁴Kavli Institute at Cornell for Nanoscale Science, Cornell University, Ithaca, New York 14853, USA.

We move the graphene along the surface or peel it up entirely by pushing a sharp probe tip into the gold pads or against the graphene itself (Fig. 1b–d and Supplementary Video 1). The graphene's elastic behaviour is reminiscent of that of thin paper: it folds and crumples out of plane, but does not notably stretch in plane (Fig. 1b). The process is almost entirely reversible in the presence of surfactants, even after considerable crumpling of the graphene.

The mechanical properties relevant for kirigami are captured by the Föppl–von Kármán number^{7,8} for a square sheet of side length L and thickness t : $\gamma = Y_{2D}L^2/\kappa \approx (L/t)^2$, that is, the ratio between the two-dimensional Young's modulus Y_{2D} and the out-of-plane bending stiffness κ , multiplied by the length squared. To determine γ , we measure κ by using the photon pressure from an infrared laser to apply a known force to a pad attached to a graphene cantilever and measuring the resulting displacement (Fig. 2a). We also measure thermal fluctuations of cantilevers to determine their spring constants (Fig. 2b and Extended Data Fig. 4), which, according to the equipartition theorem, are $k = k_B T / \langle x_{th}^2 \rangle$, where T is temperature, k_B is Boltzmann's constant, and $\langle x_{th}^2 \rangle$ is the time-averaged square of the cantilever thermal fluctuation amplitude. Although the presence of water (the aqueous solution in which the device is immersed) slows down the fluctuations, it does not change the spring constant^{15,16}. Cantilevers with lengths of 8–80 μm and widths of 2–15 μm have spring constants of 10^{-5} – 10^{-8} N m^{-1} . These are astonishingly soft springs, as many as eight orders of magnitude softer than a typical atomic force microscope cantilever. The bending stiffness κ is inferred from the measured spring constant using $k = 3\kappa W/L^3$, where W and L are the width

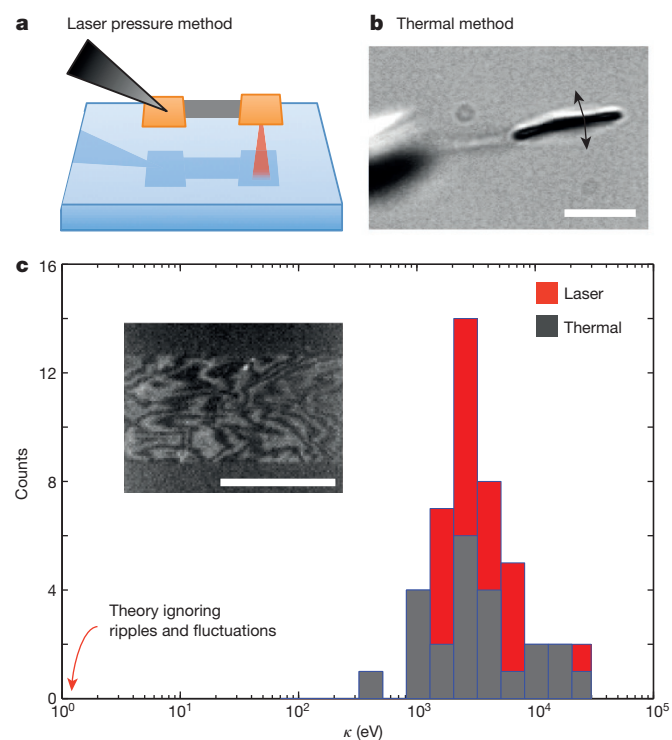


Figure 2 | Measuring the bending stiffness of monolayer graphene.

a, Applying controlled forces to a gold pad using an infrared laser. The grey triangle represents the probe tip that holds the device up off the surface; the red triangle represents the focused laser beam. The cantilever displacement gives the spring constant. **b**, Tracking the motion of a rotated device under thermal fluctuations provides an independent measurement of the spring constant (Extended Data Fig. 3). **c**, Stacked histogram of bending stiffness, and interference micrographs of devices whose aluminium release layer has been etched away, showing the structure of static ripples (inset). The spring constant relates to the bending stiffness as $k = 3\kappa W/L^3$. The red arrow points to the microscopic bending stiffness, $\kappa_0 = 1.2$ eV. Scale bars are 10 μm . Interference images were averaged over 180 frames at 90 frames per second.

and length of the cantilevers, respectively. The values obtained from these thermal measurements and the laser measurements are shown in Fig. 2c, and are seen to be orders of magnitude higher than $\kappa_0 = 1.2$ eV, which is the value that is predicted from the microscopic bending stiffness of graphene (known from simulations¹⁷ and measurements of the phonon modes in graphite¹⁸).

Both thermal fluctuations and static ripples are predicted to notably stiffen ultrathin crystalline membranes^{9–13,19,20} by effectively thickening the membrane, similar to how a crumpled sheet of paper is more rigid than a flat one. For static ripples, the effective bending stiffness is predicted to be⁹ $\kappa_{\text{eff}}/\kappa_0 \approx \sqrt{Y_{2D}\langle z_{\text{eff}}^2 \rangle}/\kappa_0$, where $\langle z_{\text{eff}}^2 \rangle$ is the space-averaged square of the effective amplitude of the static ripples and $Y_{2D} = 340$ N m^{-1} is the two-dimensional Young's modulus³. For an initially flat membrane with thermal fluctuations, the stiffness is predicted to be $\kappa_{\text{eff}} \approx \kappa_0(W/l_c)^\eta$, where $l_c = \sqrt{32\pi^3\kappa_0^2/(3Y_{2D}k_B T)}$ is the Ginzburg length¹⁹, and η is a scaling exponent.

We look for static ripples in graphene cantilevers using interference microscopy²¹ (inset of Fig. 2c). The black bands in such images are regions of constant elevation, with the spacing between black and white bands corresponding to changes in z of $\lambda/4 \approx 100$ nm (where λ is the wavelength, corrected for the refractive index of water). With a typical $\langle z_{\text{eff}}^2 \rangle$ value from these measurements of about $(100 \text{ nm})^2$, we obtain an effective bending stiffness of $\kappa_{\text{eff}}/\kappa_0 \approx 4,000$.

Static ripples are present only after releasing graphene from the surface (Extended Data Fig. 2), and likely to be sample specific and influenced by growth, fabrication details, and so on. Developing growth and fabrication protocols that can change the amplitude of the static ripples or eliminate them altogether is of great interest. Other groups have observed ripples in suspended (strained) graphene membranes^{5,22}, although they occur at a much smaller scale and their origin remains a subject of debate. Moreover, the thermal theory outlined above predicts a bending stiffness at room temperature due to thermal fluctuations of $\kappa_{\text{eff}}/\kappa_0 \approx 1,000$ for an initially flat membrane. These contradictory findings call for future experiments to firmly establish the relative contribution to bending stiffness of thermal fluctuations and static ripples²³. But irrespective of cause, the high bending stiffness notably changes the effective γ value, $\gamma_{\text{eff}} = Y_{\text{eff}}L^2/\kappa_{\text{eff}}$. With the predicted renormalization^{9,11} of Y_{eff} , we find that γ_{eff} is of the order of 10^5 – 10^7 for a sheet of graphene $10 \mu\text{m} \times 10 \mu\text{m}$ in size, close to that of a standard sheet of paper.

The mechanical similarity between graphene and paper makes it easy to translate ideas and intuition directly from paper models to graphene devices. For example, the highly stretchable graphene transistors in Fig. 3b, c and Supplementary Video 2 are based on a simple kirigami pattern of alternating, offset cuts and are created using photolithography. Here, the elasticity of the kirigami spring is determined by the pattern of cuts and the bending stiffness (rather than the Young's modulus) of the graphene. As the reconstruction of the three-dimensional shape of a stretched and lifted device in Fig. 3e shows, the graphene strips pop up and bend out of plane as the spring is stretched.

We measure the electrical response of these stretchable transistors by gating them with an approximately 10 mM KCl solution²⁴ (see Methods for details). Figure 3d plots the liquid-gate dependence of the conductance at a source–drain bias of 100 mV for a device in its initial unstretched state (blue) and when stretched by 240% (orange). The normalized change in conductance with gate voltage per graphene square is 0.7 mS V^{-1} and the resistance per graphene square at the Dirac point is 12 k Ω , comparable to what has been reported for electrolyte-gated graphene transistors²⁴. Because the graphene lattice itself is not much strained when the kirigami spring is extended, we do not expect or observe a notable change in the conductance curves between the unstretched and stretched states, which is highly desirable for stretchable electronics²⁵. Furthermore, stretching and unstretching a similar device more than 1,000 times did not substantially change its electrical properties.

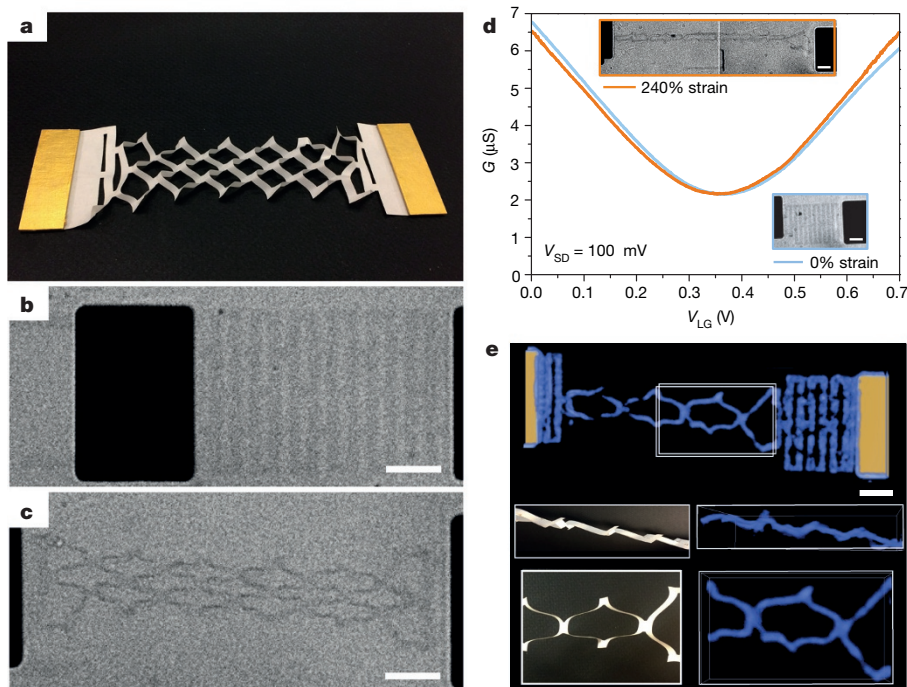
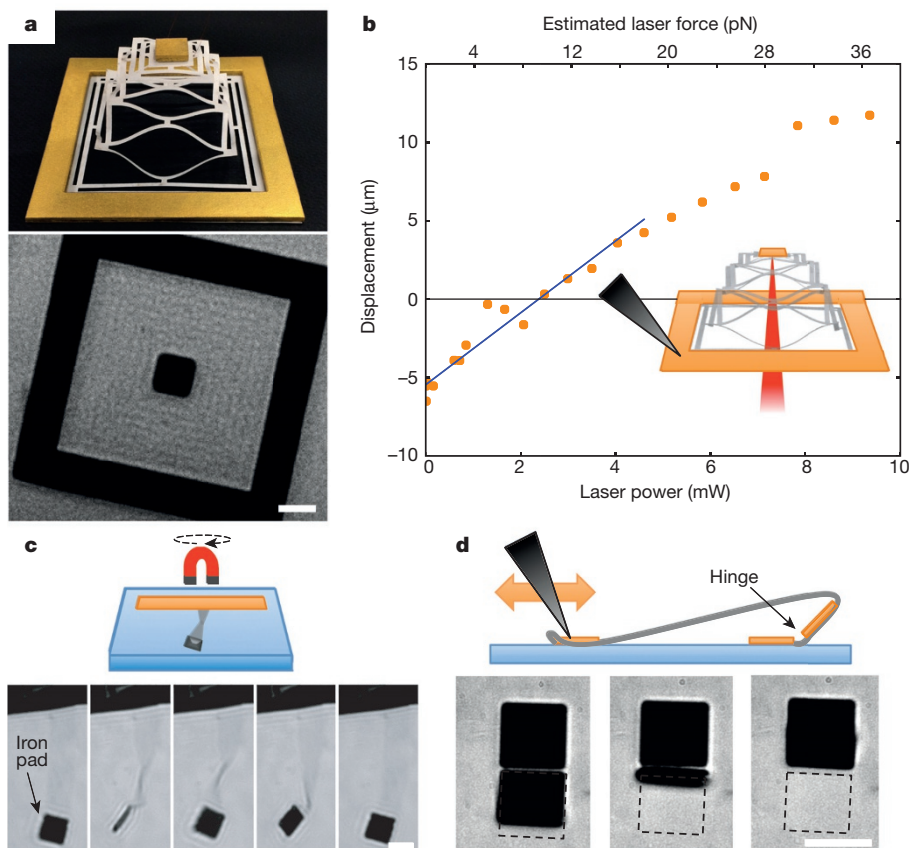


Figure 4a and Supplementary Video 3 show graphene cut so that it forms an out-of-plane pyramidal spring, along with a paper model. The spring's force–distance curve in Fig. 4b, measured with the photon pressure from an infrared laser focused on the central pad, gives a spring constant of $k = 2 \times 10^{-6} \text{ N m}^{-1}$. This value compares well with the spring constant estimate of (5×10^{-7}) – $(5 \times 10^{-6}) \text{ N m}^{-1}$, obtained from our κ measurements (Fig. 2) and the geometry of the device.

Remote actuation of the kirigami devices is possible using magnetic fields or linked graphene elements. Figure 4c illustrates magnetic actuation, with magnetic forces and torques acting on an attached iron pad allowing for parallel (many hinges being controlled simultaneously) and complex manipulations to be made. The opening and closing of the graphene hinge (which is 1 μ m long and 10 μ m wide) in Fig. 4d uses a longer graphene strip (out of focus in the image) that extends in



a loop over the hinge to a gold pad, so that moving this probe along the surface opens and closes the hinge (Supplementary Video 3). Although the hinge is only one atom thick, it survived more than 10,000 open-and-close cycles (at which point the gold pads started to warp). This remarkable resilience and the scope for scaling down to tens of nanometres make monolayer graphene hinges ideally suited for use in microscale moving parts.

We envisage that graphene kirigami will have many useful applications. For example, springs like those in Figs 3 and 4 are easily designed, with spring constants that range from 1 N m^{-1} to 10^{-8} N m^{-1} (which covers the full range from atomic force microscopes to optical traps), for use as force measurement devices with a simple visual readout and femtonewton force resolution. The addition of elements such as bimorphs²⁶ or chemical tags to graphene kirigami devices²⁷ will create environment-responsive metamaterials. Kirigami techniques can also easily be applied to other two-dimensional materials that have different optical, electronic, and mechanical properties, which creates opportunities for further development of self-actuated two-dimensional functional devices that respond to light or magnetic fields, changes in temperature, or chemical signals. Such atomically thin membrane devices may be used for sensing, manipulation, complex origami, and nanoscale robotics.

Online Content Methods, along with any additional Extended Data display items and Source Data, are available in the online version of the paper; references unique to these sections appear only in the online paper.

Received 10 March; accepted 14 May 2015.

Published online 29 July 2015.

- Wang-Iverson, P., Lang, R. J. & Yim, M. (eds) *Origami 5: Fifth International Meeting of Origami Science, Mathematics, and Education* (CRC Press, 2011).
- Hawkes, E. *et al.* Programmable matter by folding. *Proc. Natl Acad. Sci. USA* **107**, 12441–12445 (2010).
- Lee, C., Wei, X., Kysar, J. W. & Hone, J. Measurement of the elastic properties and intrinsic strength of monolayer graphene. *Science* **321**, 385–388 (2008).
- Booth, T. J. *et al.* Macroscopic graphene membranes and their extraordinary stiffness. *Nano Lett.* **8**, 2442–2446 (2008).
- Meyer, J. C. *et al.* The structure of suspended graphene sheets. *Nature* **446**, 60–63 (2007).
- Bunch, J. S. *et al.* Electromechanical resonators from graphene sheets. *Science* **315**, 490–493 (2007).
- Föppl, A. *Vorlesungen über technische Mechanik* (B. G. Teubner, 1905).
- von Kármán, T. *Festigkeitsproblem im Maschinenbau*. Vol. 4 (Encyklopädie der Mathematischen Wissenschaften, 1910).
- Košmrlj, A. & Nelson, D. R. Mechanical properties of warped membranes. *Phys. Rev. E* **88**, 012136 (2013).
- Nelson, D. R. & Peliti, L. Fluctuations in membranes with crystalline and hexatic order. *J. Phys.* **48**, 1085–1092 (1987).
- Aronovitz, J. A. & Lubensky, T. C. Fluctuations of solid membranes. *Phys. Rev. Lett.* **60**, 2634–2637 (1988).
- Le Doussal, P. & Radzihovsky, L. Self-consistent theory of polymerized membranes. *Phys. Rev. Lett.* **69**, 1209–1212 (1992).
- Los, J. H., Katsnelson, M. I., Yazyev, O. V., Zakharchenko, K. V. & Fasolino, A. Scaling properties of flexible membranes from atomistic simulations: application to graphene. *Phys. Rev. B* **80**, 121405 (2009).
- Li, X. *et al.* Large-area synthesis of high-quality and uniform graphene films on copper foils. *Science* **324**, 1312–1314 (2009).
- Velasco, S. On the Brownian motion of a harmonically bound particle and the theory of a Wiener process. *Eur. J. Phys.* **6**, 259–265 (1985).
- te Velthuis, A. J. W., Kerssemakers, J. W. J., Lipfert, J. & Dekker, N. H. Quantitative guidelines for force calibration through spectral analysis of magnetic tweezers data. *Biophys. J.* **99**, 1292–1302 (2010).
- Fasolino, A., Los, J. H. & Katsnelson, M. I. Intrinsic ripples in graphene. *Nature Mater.* **6**, 858–861 (2007).
- Nicklow, R., Wakabayashi, N. & Smith, H. G. Lattice dynamics of pyrolytic graphite. *Phys. Rev. B* **5**, 4951–4962 (1972).
- Roldán, R., Fasolino, A., Zakharchenko, K. V. & Katsnelson, M. I. Suppression of anharmonicities in crystalline membranes by external strain. *Phys. Rev. B* **83**, 174104 (2011).
- Braghin, F. L. & Hasselmann, N. Thermal fluctuations of free-standing graphene. *Phys. Rev. B* **82**, 035407 (2010).
- Georgiou, T. *et al.* Graphene bubbles with controllable curvature. *Appl. Phys. Lett.* **99**, 093103 (2011).
- Wang, W. L. *et al.* Direct imaging of atomic-scale ripples in few-layer graphene. *Nano Lett.* **12**, 2278–2282 (2012).
- Košmrlj, A. & Nelson, D. R. Thermal excitations of warped membranes. *Phys. Rev. E* **89**, 022126 (2014).
- Chen, D., Tang, L. & Li, J. Graphene-based materials in electrochemistry. *Chem. Soc. Rev.* **39**, 3157–3180 (2010).
- Rogers, J. A., Someya, T. & Huang, Y. Materials and mechanics for stretchable electronics. *Science* **327**, 1603–1607 (2010).
- Zhu, S.-E. *et al.* Graphene-based bimorph microactuators. *Nano Lett.* **11**, 977–981 (2011).
- Yuk, J. M. *et al.* Graphene veils and sandwiches. *Nano Lett.* **11**, 3290–3294 (2011).

Supplementary Information is available in the online version of the paper.

Acknowledgements We thank D. Nelson, M. Bowick, A. Kosmrlj, J. Alden, A. van der Zande, and R. Martin-Wells for discussions. We thank E. Minot for assistance with electrolyte gating. We thank R. Hovden for discussions on three-dimensional reconstruction theory and techniques, and R. Hovden, M. Hanwell, and U. Ayachit for developing and supporting the TomViz three-dimensional visualization software. We thank J. Wardini, P. Ong, A. Zaretski, and S. P. Wang for additional graphene samples, and F. Parish with Cornell's College of Architecture, Art, and Planning for assistance with the paper models. We also acknowledge the Origami Resource Center (<http://www.origami-resource-center.com/>) for kirigami design ideas. This work was supported by the Cornell Center for Materials Research (National Science Foundation, NSF, grant DMR-1120296), the Office of Naval Research (N00014-13-1-0749), and the Kavli Institute at Cornell for Nanoscale Science. Devices were fabricated at the Cornell Nanoscale Science and Technology Facility, a member of the National Nanotechnology Infrastructure Network, which is supported by the NSF (ECCS-0335765). K.L.M. and P.Y.H. acknowledge support from the NSF Graduate Research Fellowship Program (DGE-1144153 and DGE-0707428). Tomography visualization software development was supported by a SBIR grant (DE-SC0011385).

Author Contributions Device design and actuation techniques were developed by M.K.B., A.W.B., P.A.R., S.P.R., and K.L.M. under the supervision of P.L.M. Fabrication and characterization was performed by the above authors with additional support from A.R.R., J.W.K., and B.K. Bending stiffness measurements were designed by A.W.B. and P.L.M. and carried out by M.K.B., P.A.R., and K.L.M. with data analysis by S.P.R., A.W.B., M.K.B., K.L.M., and P.A.R. under the supervision of P.L.M. Electrical measurements were performed by K.L.M. and M.K.B. under the supervision of P.L.M. Three-dimensional reconstructions were performed by P.Y.H. under the supervision of D.A.M. The paper was written by M.K.B. and P.L.M., with assistance from P.A.R., A.W.B., K.L.M., and P.Y.H. and in consultation with all authors.

Author Information Reprints and permissions information is available at www.nature.com/reprints. The authors declare no competing financial interests. Readers are welcome to comment on the online version of the paper. Correspondence and requests for materials should be addressed to P.L.M. (p1m23@cornell.edu).

METHODS

Graphene growth. We grow graphene on copper following a standard chemical vapour deposition process¹⁴. The copper foil is purchased from Alpha Aesar, stock number 13382. The copper is annealed for 36 min at 980 °C with a H₂ flow of 60 standard cubic centimetres per minute (s.c.c.m.). Graphene is grown at 980 °C for 20 min with a H₂ flow of 60 s.c.c.m. and a CH₄ flow of 36 s.c.c.m. The foil is then cooled in a matching environment as quickly as possible.

Graphene characterization. Typical Raman spectra, scanning electron microscope images, and bright-field transmission electron microscope (TEM) images all confirm that the growths yielded mostly single-layer graphene with small bilayer regions (Extended Data Fig. 1). Dark-field TEM on a variety of growths reveal that typical grain sizes are of the order of hundreds of nanometres to micrometres.

Fabrication of cantilevers and kirigami devices. Fabrication follows standard graphene processing methods, with the addition of an aluminium release layer. We evaporate 40 nm of aluminium on 170- μm double-side-polished fused silica wafers from Mark Optics. We dice the wafers into 2 cm \times 2 cm chips, and transfer graphene to the chips using 2% poly(methyl methacrylate) (PMMA). We then etch the copper in ferric chloride (Transene, CE-200) for one hour and rinse with five consecutive deionized water baths. We transfer the graphene onto the aluminium-coated chip, and soak overnight in acetone to remove the PMMA. Next, we use photolithography to pattern the pads and evaporate 50 nm of gold. We pattern the graphene strips and etch away the unwanted graphene with a 25-s oxygen plasma. Finally, we soak the chip in a mild (10:1) deionized water/HCl solution until the aluminium release layer has completely disappeared. The chip is transferred directly to a deionized water bath, which is kept refrigerated between uses to discourage bacterial growth.

Atomic force microscope characterization. Atomic force microscope measurements on aluminium-free chips that are run in parallel with measured devices usually give step heights of 1–3 nm above that of pristine exfoliated graphene (Extended Data Fig. 2). Although it is impossible to completely avoid polymer residues from standard transfer and fabrication processing, a 2-nm layer of the stiffest PMMA (Young's modulus $Y = 3.3$ GPa, Poisson ratio $\sigma = 0.4$) should add only about 20 eV to the stiffness (since $\kappa = Yt^3/[12(1-\sigma)]$), which is negligible compared to the measured values.

Influence of surfactants. The addition of a surfactant reduces the graphene's adhesion to the surface and prevents the graphene from permanently sticking to itself. We performed bending stiffness measurements with and without surfactant, and found that the presence of surfactant does not measurably affect the bending stiffness. A surfactant was used in all kirigami experiments. We used sodium dodecylbenzenesulfonate (SDBS) from Sigma-Aldrich (product number 289957), dissolved in deionized water to a concentration of approximately 3 mM. During the measurement process some water evaporates and is replaced with deionized water, so that the concentration of SDBS remains approximately constant over time.

Extraction of $\langle x_{\text{th}}^2 \rangle$ from thermal motion. To extract $\langle x_{\text{th}}^2 \rangle$ from the thermal motion of the gold pad on the free end of the graphene cantilever, we recorded the motion at 90 frames per second for about 20 min to ensure that the entire phase space of the cantilever motion was sampled. The first 20 s from the trace of the free gold pad on a 40 μm \times 10 μm cantilever are shown in Extended Data Fig. 3a. We tracked the motion of the pad centroid frame by frame using image analysis to extract the x position of the pad over time; the x direction is perpendicular to the profile of the free gold pad (see inset of Extended Data Fig. 3a). To extract $\langle x_{\text{th}}^2 \rangle$ from this thermal motion, we calculated the power spectral density (PSD), which is the Fourier transform of the autocorrelation of the data, shown in Extended Data

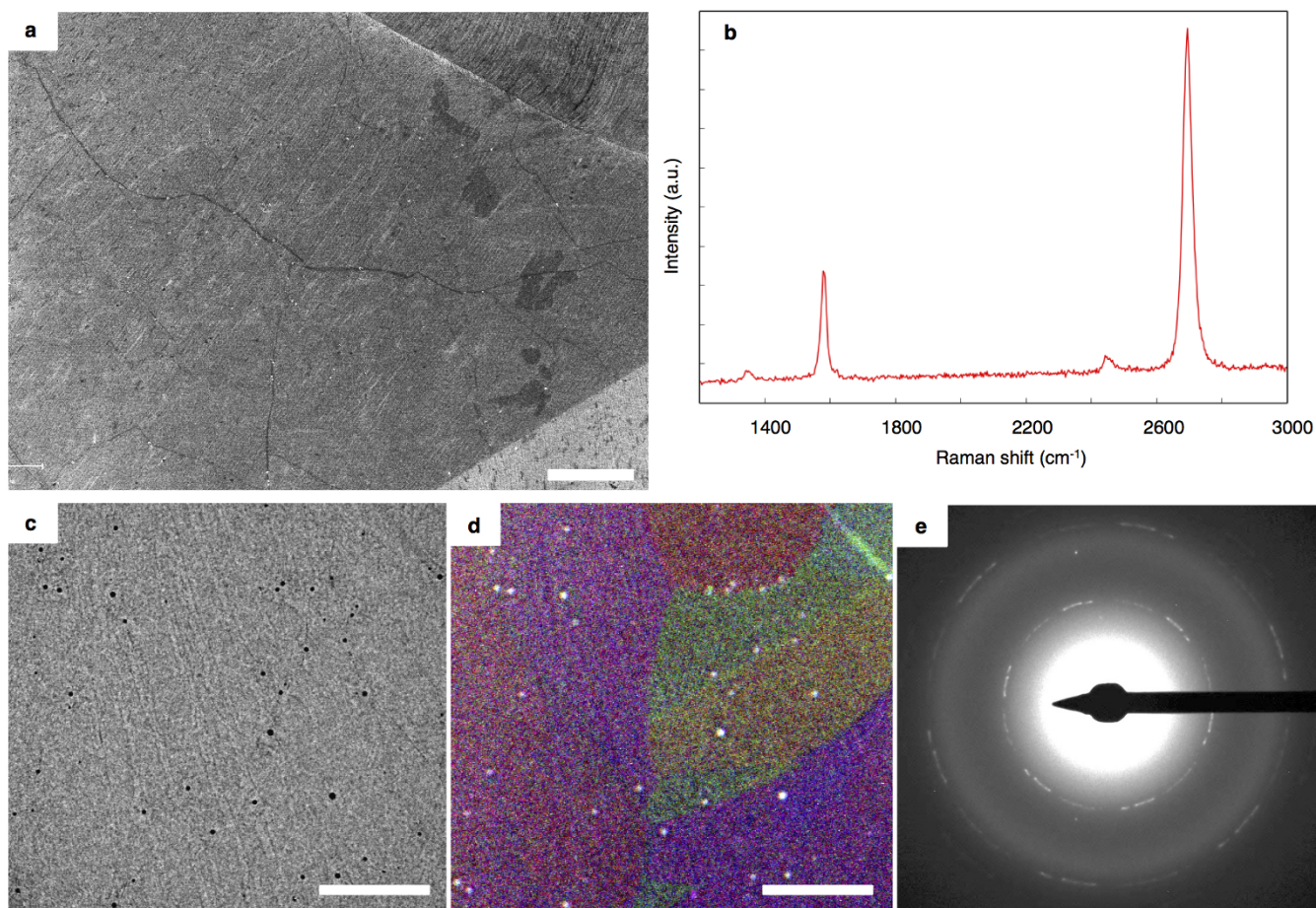
Fig. 3b. In all devices we observed low-frequency $1/f$ noise from the long-timescale motion of the supporting probe (shown in red). This low-frequency noise was excluded from further analysis. We fit the data plotted in blue, which resulted from the thermal motion of the free gold pad, with the theoretical one-sided PSD for Brownian thermal motion^{15,16} (dashed line): $S_{xx}(f) = S_0/[1 + (ff_c)^2]$, where S_0 is the low-frequency value of the Brownian motion PSD, and f_c is the corner frequency. The integral of this fitted function yields^{15,16} $\langle x_{\text{th}}^2 \rangle: \int_0^\infty S_{xx}(f) df = \langle x_{\text{th}}^2 \rangle$. Using $k = k_B T / \langle x_{\text{th}}^2 \rangle$, where $\langle x_{\text{th}}^2 \rangle = (130 \text{ nm})^2$ for the device shown in Extended Data Fig. 3, we find that the spring constant for this 40 μm \times 10 μm cantilever is $k = 2.4 \times 10^{-7} \text{ N m}^{-1}$ and that the bending stiffness $\kappa = 3 \text{ keV}$.

Interferometric measurements. The wavelength of the laser that was used for the interferometric measurements is 436 nm; in water this means that the separation of the black and white bands is $436/4/1.33 = 82 \text{ nm}$. We used a 10-nm full-width-half-maximum bandpass filter with a centre wavelength of 430 nm on the 436-nm line of a mercury arc lamp. The reflectivity of the glass–water–graphene–water cavity creates a situation where the reflectivity changes from 0.0026 to 0.0067 between dark and light bands (based on thin-film equations). A single sheet of graphene in water has a reflectivity of 0.0002, so our geometry greatly enhances the visibility of graphene.

Electrical measurements of stretchable transistors. Electrical measurements were conducted in an approximately 10 mM KCl solution, with a few drops of about 3 mM SDBS solution added. Since water evaporates during the measurement process, we periodically add deionized water to keep the concentration of SDBS approximately constant. The solution was gated by a gold wire, and the gate–drain current was minimized by contacting the drain electrode with a parylene-C-coated tungsten probe. An Ithaco 1211 current preamplifier was used to measure the current, and the system had a negligible gate–drain leakage current of about 10 nA. The device geometry in Fig. 3d is equivalent to approximately 40 squares in series.

Laser force actuation and calibration. Force–displacement curves for cantilevers and a pyramid were measured using the radiation pressure of a 1,064-nm laser. The spring constant was determined by finding the slope of a linear fit to the data. The power of the laser was adjusted using an acousto-optic modulator. The force delivered to a gold pad was calibrated experimentally using the known weight of the gold. For a given power, the laser was focused near the centre of the gold pad, and the change in displacement was measured using a piezo attached to the objective of the optical microscope.

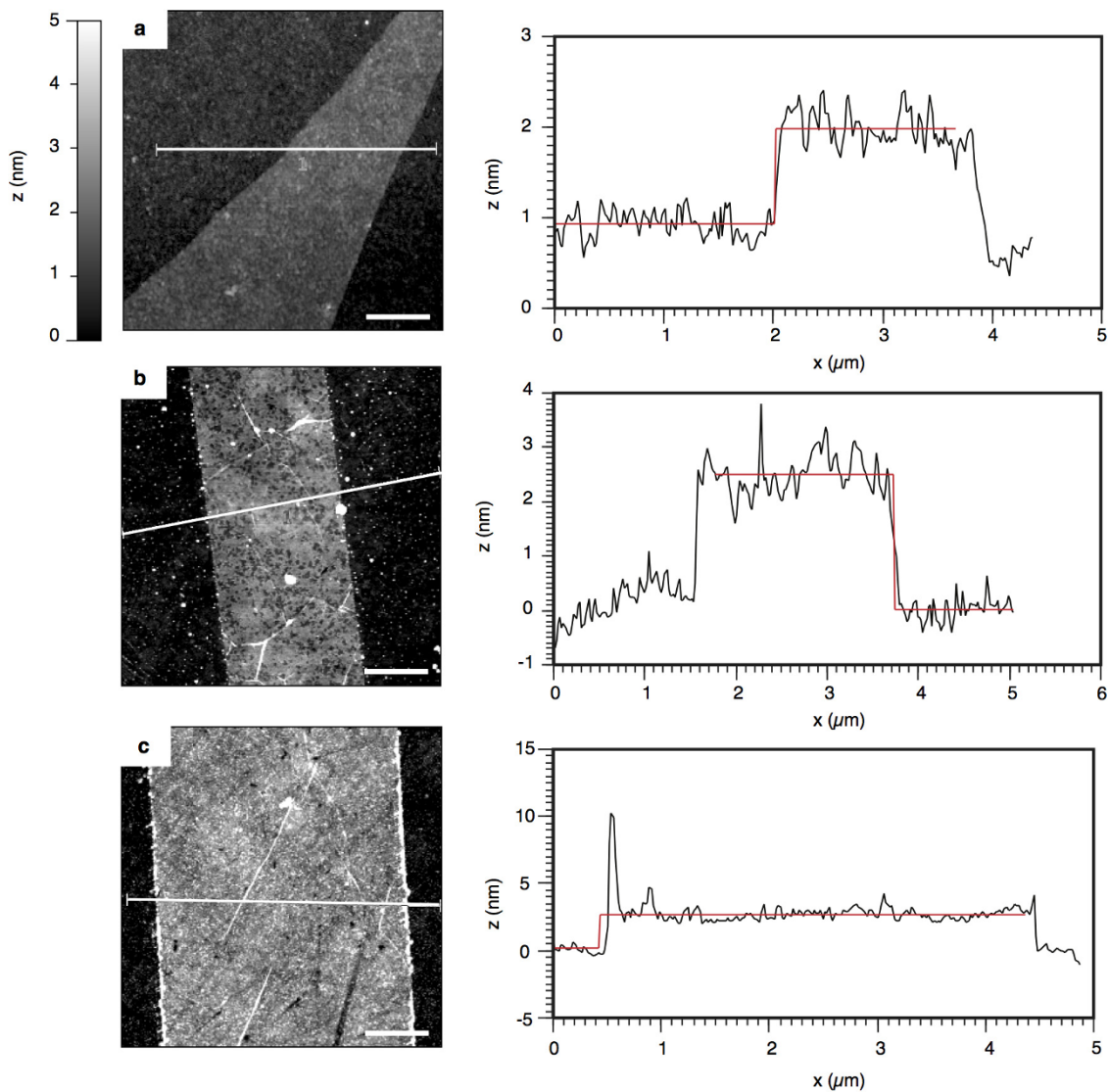
Three-dimensional reconstruction of kirigami devices. We reconstructed the three-dimensional shape of graphene kirigami devices from a z-scanned focal series (Supplementary Video 2). We first acquire a series of images, varying the position of the lens to scan through a z depth of 100 μm in 10-nm steps. The images are background-subtracted to remove fixed-pattern features on the lens and camera. We then find the focal plane of each x – y pixel by using a refined minimum-intensity algorithm to look for the z plane with the highest contrast. Because the graphene is much thinner than the depth of focus, we assume it behaves like a point object in the z direction. In this model, we use Gaussian fits to find the z centre of the dip in intensity for each x – y pixel. For graphene near the gold pads, we restrict the fit positions to exclude shadowing effects from the pads as they go out of focus. The resulting matrix of z positions is cropped to the size of our object, converted to a three-dimensional matrix of intensities, and smoothed with a three-dimensional Gaussian blur of about 400 nm to reduce noise. Finally, we use TomViz (a development of Paraview that is optimized for tomography visualizations) to render the three-dimensional object. The colour map is based on the intensity of the original video.



Extended Data Figure 1 | Characterization of representative graphene.

a, Scanning electron microscope image of chemical vapour deposition graphene on copper foil. All the graphene used in these experiments was predominantly single-layer, with some small bilayer patches. The larger-scale contrast variations show the copper grains. Scale bar is 10 μm . **b**, Raman spectrum of chemical vapour deposition graphene transferred to SiO_2/Si (285-nm oxide layer) substrate. The spectrum shows graphene's characteristic G peak at $1,580\text{ cm}^{-1}$ and two-dimensional peak at $2,700\text{ cm}^{-1}$; the ratio

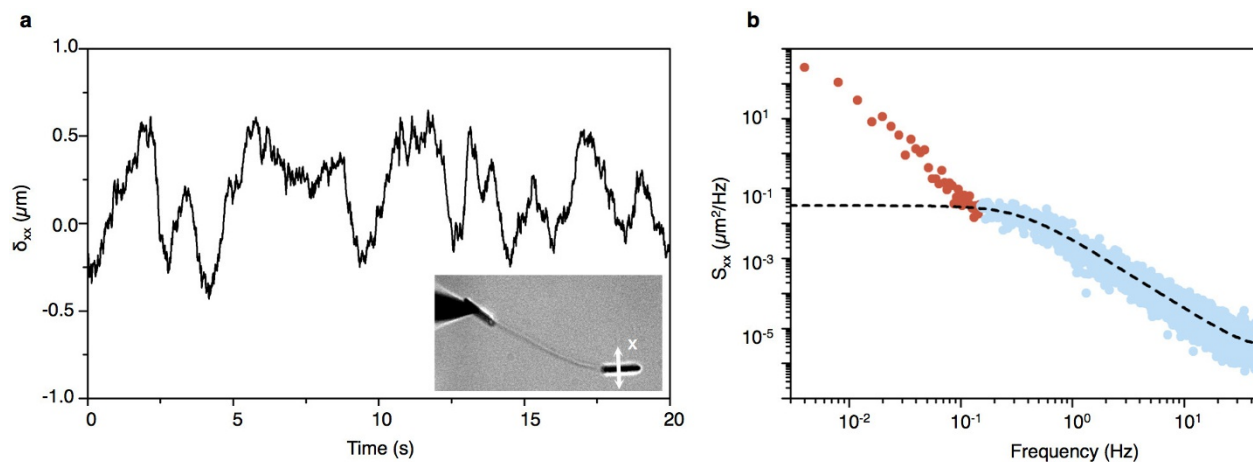
between the two indicates that the graphene is primarily monolayer. A small D peak at $1,350\text{ cm}^{-1}$ indicates low disorder. The small peak at $2,450\text{ cm}^{-1}$ is background. **c**, High-contrast bright-field TEM image of graphene transferred over 10-nm-thick Si_3N_4 windows shows continuous monolayer graphene. Scale bar is 1 μm . **d**, False-colour composite image of dark-field TEM images showing grain size and shape. The graphene is polycrystalline, with grain sizes of the order of micrometres. Scale bar is 1 μm . **e**, TEM diffraction pattern for region shown in **c** and **d**.



Extended Data Figure 2 | Atomic force microscopy of graphene.

a, Exfoliated, unprocessed monolayer graphene. Step height along the red line shown on the height (z) map is 1.0 ± 0.3 nm. **b**, **c**, Representative data from aluminium-free chips that are run in parallel with the devices used in bending stiffness measurements. Step heights are 2.5 ± 0.4 nm and 2.4 ± 0.5 nm.

Chips that look clean under the optical microscope typically have 2–4 nm total step heights. We occasionally see higher residue lines at the edges of the graphene, as in **c**. The PMMA residue is not sufficiently thick to explain the notably increased bending stiffness of the graphene (see Methods). Scale bars are 1 μ m.

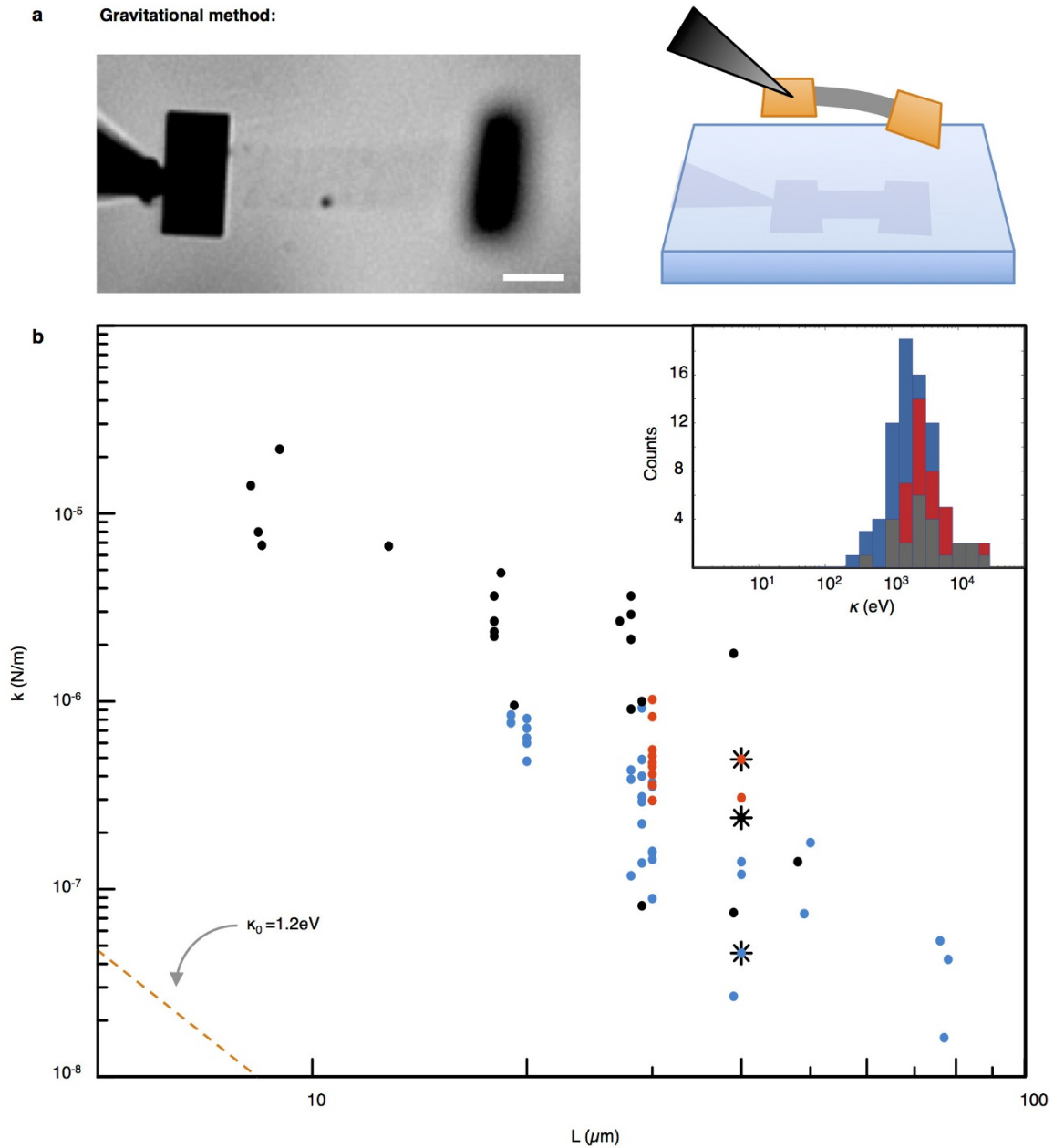


Extended Data Figure 3 | Thermal motion of graphene cantilever gold pads.

a, Time trace of the x position of the gold pad centroid on a $40\ \mu\text{m} \times 10\ \mu\text{m}$ graphene cantilever, showing the first 20 s of a 20-min trace. The x direction is perpendicular to the profile of the gold pad, as indicated in the inset.

b, PSD (S_{xx}) of the full 20-min time trace from **a**. The blue data points were included in the fit to the Brownian motion PSD function (dashed line); the red

data points from about 10^{-3} Hz to about 10^{-1} Hz were excluded, because they show considerable $1/f$ noise as a result of the motion of the probe holding the cantilever. We integrate the fitted function S_{xx} to determine $\langle x_{\text{th}}^2 \rangle$. For the device shown, $\langle x_{\text{th}}^2 \rangle = (130\ \text{nm})^2$, the spring constant $k = 2.4 \times 10^{-7}\ \text{N m}^{-1}$, and the bending stiffness $\kappa = 3\ \text{keV}$.



Extended Data Figure 4 | Bending stiffness measurements. **a**, We also performed a rough measurement of the spring constant using the force of gravity on the gold pads. After lifting the cantilever off the surface, the vertical deflection x_g is determined using the shallow depth of focus of the microscope, adjusted for the change in index of refraction. The gravitational force F_g (corrected for buoyancy) yields the spring constant: $k = F_g/x_g$. For the 50- μm -long cantilever shown (scale bar is 10 μm) with a 2-pN gold pad and $x_g = 25 \mu\text{m}$, we find that $k = 8 \times 10^{-8} \text{N m}^{-1}$. We repeated the measurement for a variety of devices of varying length L and width $W = 10 \mu\text{m}$. We have

observed that the cantilevers sometimes curve downwards even in the absence of an applied force, presumably due to residual materials or strains in the graphene, so these gravitational measurements probably have a systematic offset. **b**, The measured spring constants of 10- μm -wide devices are shown on a plot of spring constant versus device length for the thermal fluctuation (black), gravitational deflection (blue), and laser force measurements (red). The data from all three techniques (plus additional laser data for devices with other widths, as in Fig. 2) are shown in the inset as a histogram. Data with stars are from the same device, using the three different measurement techniques.